

Super-Clausius–Clapeyron scaling of extreme precipitation explained by shift from stratiform to convective rain type

Received: 19 December 2023

Nicolas A. Da Silva ^{1,2}✉ & Jan O. Haerter ^{1,2,3,4}

Accepted: 25 March 2025

Published online: 28 April 2025

 Check for updates

Short-duration precipitation extremes pose a risk to human lives and infrastructure and may be strongly affected by climate change. In the past two decades, several studies reported that extreme rainfall intensity can increase with temperature at rates exceeding the thermodynamic Clausius–Clapeyron rate. Two explanations have been proposed for this: (1) convective precipitation—arising from thunderstorms—might be strongly invigorated with temperature; (2) a statistical shift from low-intensity stratiform rainfall to higher-intensity convective rainfall might amplify the scaling rate with temperature. Here we use high spatio-temporal-resolution lightning records in Europe to test these two hypotheses at the storm scale, that is, within 5 km spatially and 10 min temporally. We show that the statistical shift in rain type alone accounts for the observed super-Clausius–Clapeyron scaling rate, and when considered in isolation, both stratiform and convective precipitation extremes increase at the Clausius–Clapeyron rate—thus refuting hypothesis (1). Mesoscale convective systems, which play a dominant role in generating precipitation extremes, do feature a super-Clausius–Clapeyron scaling rate because of a substantial increase in their convective fraction with dew point temperature above 14 °C. Analyses of intensity–duration–frequency curves show that extreme sub-hourly storms are the most strongly intensified with higher dew point temperatures.

Understanding the mechanisms leading to short-duration precipitation extremes is critical in assessing societal impacts, such as those resulting in flash floods^{1–3}, and the potential frequency increase of such events in a warmer climate^{4–7}. A robust finding in climate models is that relative humidity is nearly constant in future climate projections^{8–10}. If so, specific humidity will vary with saturation vapour pressure as given by the Clausius–Clapeyron (CC) relation. A long-standing hypothesis is that precipitation extremes might increase at a rate close to the approximate 7% K⁻¹ predicted by the CC relation for typical near-surface temperatures^{8,9}.

However, short-duration precipitation extreme scaling rates exceeding the CC rate were reported for several mid-latitude^{11–14} and tropical regions^{15,16} and even replicated in certain simulations^{17,18}. Other work^{19–21} cautioned that an apparent super-CC scaling could be the result of a statistical shift in precipitation type from weak stratiform precipitation—resulting from large frontal precipitation bands at low temperatures—to intrinsically more intense thunderstorm precipitation at higher temperatures.

Yet the inherent mechanisms underlying convection were suggested to be capable of bringing about such disproportionate scaling²².

¹Complexity and Climate, Leibniz Centre for Tropical Marine Research, Bremen, Germany. ²Department of Physics and Astronomy, University of Potsdam, Potsdam, Germany. ³Niels Bohr Institute, University of Copenhagen, Copenhagen, Denmark. ⁴School of Science, Constructor University Bremen, Bremen, Germany. ✉e-mail: dasilvanicolas95@gmail.com

Indeed, conditioning on times and regions with predominantly convective activity, super-CC scaling of precipitation extremes was described in several areas^{12–14,23}. These findings were interpreted in a way that, beyond possible statistical effects, the super-CC scaling of extreme precipitation might indeed have a physical, mechanistic origin⁷.

All observational studies reporting super-CC scaling of extreme convective precipitation discriminated convective from stratiform precipitation at a relatively low spatio-temporal resolution on the order of a few hours and hundreds of kilometres (refs. 12–14,23). More specifically, Berg et al. (2013)²³ used 3-hourly surface synoptic observations of cloud types at approximately 50-km spatial resolution to classify convective and stratiform precipitation over Germany. Related work defined convective precipitation on a precipitation event basis¹², selecting precipitation events for which at least one lightning strike was detected during the event and within 30 km of the station location. Ivancic and Shaw (2016)¹³ defined convective precipitation similarly, namely as precipitation occurring during a day with lightning activity reported at a maximal distance of 32 km from their station locations. Park and Min (2017)¹⁴ adopted a method similar to that of Berg et al. (2013)²³, using the most dominant observed cloud type during a 3-h time window to determine the precipitation type. However, convective and stratiform precipitation types often occur at much higher spatio-temporal variability and the two types generally coexist within the same precipitation system²⁴. In particular, long-lived mesoscale convective systems (MCSs) typically span several hundred kilometres in diameter²⁵, dominate extreme rainfall yield over Europe²⁶, contain both stratiform and convective subregions²⁷ and are projected to increase in intensity and frequency over Europe²⁸.

Here we call into question that a physical mechanism causing the super-CC scaling exists. From our lightning-based classification of convection, which we pair with high-resolution dew point temperature and precipitation observations over Germany, we conclude that super-CC increases have a purely statistical origin. We, however, describe situations where such statistical superposition may nonetheless have practical relevance, such as during MCS passages or in intensity–duration–frequency (IDF) curves.

Detecting convective precipitation at high resolution

We base our analysis on a large station network (514 stations) covering Germany (Table 1 and Fig. 1a). Both the accumulated precipitation and the dew point temperature (T_d) are recorded at 10-min intervals, in total representing 7,405 years of aggregated data between 2005 and 2020. We combine this large amount of data with the similarly high-resolution ($0.071^\circ \times 0.045^\circ$ on a longitude–latitude grid at 10-min temporal intervals) European Cooperation for Lightning Detection (EUCLID) lightning dataset to discriminate convective precipitation at an unprecedented degree of precision (Table 1). We define convective-type precipitation as accumulated precipitation during a 10-min window ($\tau_{cv} = 10$ min) during which at least one cloud-to-ground (CG) lightning flash was detected within a radius $r_{cv} = 5$ km of the station location. Conversely, we define stratiform precipitation as 10-min accumulated precipitation for which no CG lightning flash was detected within a (variable) radius r_{st} of the station location and within a $\tau_{st} = 3$ -h window centred on the starting time of the precipitation record. We take the type of the remaining precipitation data as uncertain and assume that it may contain both convective and stratiform precipitation (Methods and Extended Data Figs. 1 and 2).

The EUCLID lightning flashes generally coincide with the highest precipitation intensities (Fig. 1b), confirming their utility in identifying convective cells. Exploiting this method, we are able to cleanly separate convective from stratiform precipitation in convective environments such as during the occurrence of MCSs (Fig. 1b,c). During these events, convective precipitation may be of short duration, surrounded by stratiform precipitation and preceded by peaks in T_d fuelling the

Table 1 | Summary of datasets used

Dataset	Temporal resolution	Time range	Spatial coverage
Stations (DWD) ⁴⁴	10 min	2005–2020	514 stations
Lightning (EUCLID) ^{45,46}	10 min	2005–2020	$0.071^\circ \times 0.045^\circ$
Radar (RADOLAN, DWD) ⁴⁷	5 min	2007–2019	1 km \times 1 km
Topography (GEBCO)		2021	15"

Columns indicate the name of each dataset, its temporal resolution, the time range within which the data were analysed and the spatial coverage or resolution, respectively (Methods).

precipitation system (Fig. 1c). We match each 10-min precipitation accumulation with the maximum T_d in the 3-h time window preceding the 10-min precipitation record. This procedure allows us to derive the scaling of 10-min precipitation extremes with T_d , denoted $P_{99}(T_d)$. $P_{99}(T_d)$ for a given T_d bin is thereby defined as the 99th percentile of all 10-min intervals with accumulated precipitation exceeding a threshold of 0.1 mm (Methods).

Scalings of precipitation extremes

When enforcing a strict separation between convective and stratiform precipitation, that is, $r_{cv} = 5$ km, $\tau_{cv} = 10$ min, $r_{st} = 300$ km and $\tau_{st} = 3$ h, we find that extreme convective precipitation in fact increases with dew point temperature according to the CC relation. Similarly, $P_{99}(T_d)$ for stratiform precipitation is close to the CC relation but with a reduction of precipitation intensities by a factor of eight compared to $P_{99}(T_d)$ for convective precipitation (Fig. 2a). This factor between convective and stratiform precipitation intensity is consistent with the observed order of magnitude difference in updraught vertical velocities between convective and stratiform clouds²⁹.

Figure 2c shows the occurrence frequencies of convective, stratiform and total precipitation as a function of T_d . Consistent with previous work¹⁹, stratiform precipitation dominates at low T_d , peaking near 5°C , whereas convective precipitation peaks at higher T_d ($\approx 18^\circ\text{C}$). In fact, the contribution of convective precipitation increases approximately exponentially (at a rate $\beta \approx 41\% \text{ }^\circ\text{C}^{-1}$) from 7°C to 22°C . Thus, the gradual shift from weak stratiform to heavy convective precipitation with increasing T_d generates a purely statistical super-CC (nearly 2-CC) scaling of extreme total precipitation.

Although much less dramatic, the slight super-CC behaviour of extreme stratiform precipitation may be related to the same statistical effect as our definition of stratiform precipitation may still include a small portion of convective precipitation resulting from convective systems that do not produce any CG lightning³⁰. Whereas the slope for the stratiform type is consistent with previous studies, the non-super-CC behaviour of extreme convective precipitation reveals that the much more discriminate spatio-temporal definition of convective precipitation used here may be required to obtain accurate scaling of convective precipitation extremes with T_d .

To ensure that these findings on a simple-CC scaling of convective extremes with T_d do not depend on our particular choice of parameters, we systematically modify the percentile used for the definition of extremes (Extended Data Fig. 3), the threshold used for defining non-zero precipitation records (Extended Data Fig. 4) and compute the scalings for fixed T_d bin widths (Extended Data Fig. 5). In either case, the scaling of convective-type precipitation intensity remains within simple-CC scaling.

Due to the above strict criteria for separating convective from stratiform precipitation, about half of the precipitation events remain unclassified. We find that extreme precipitation from these unclassified events also scale as nearly CC at intermediate values between convective and stratiform extreme precipitation rates (Extended Data Fig. 6b,d). Devising a conceptual model where both convective and stratiform precipitation scale as CC (Methods and

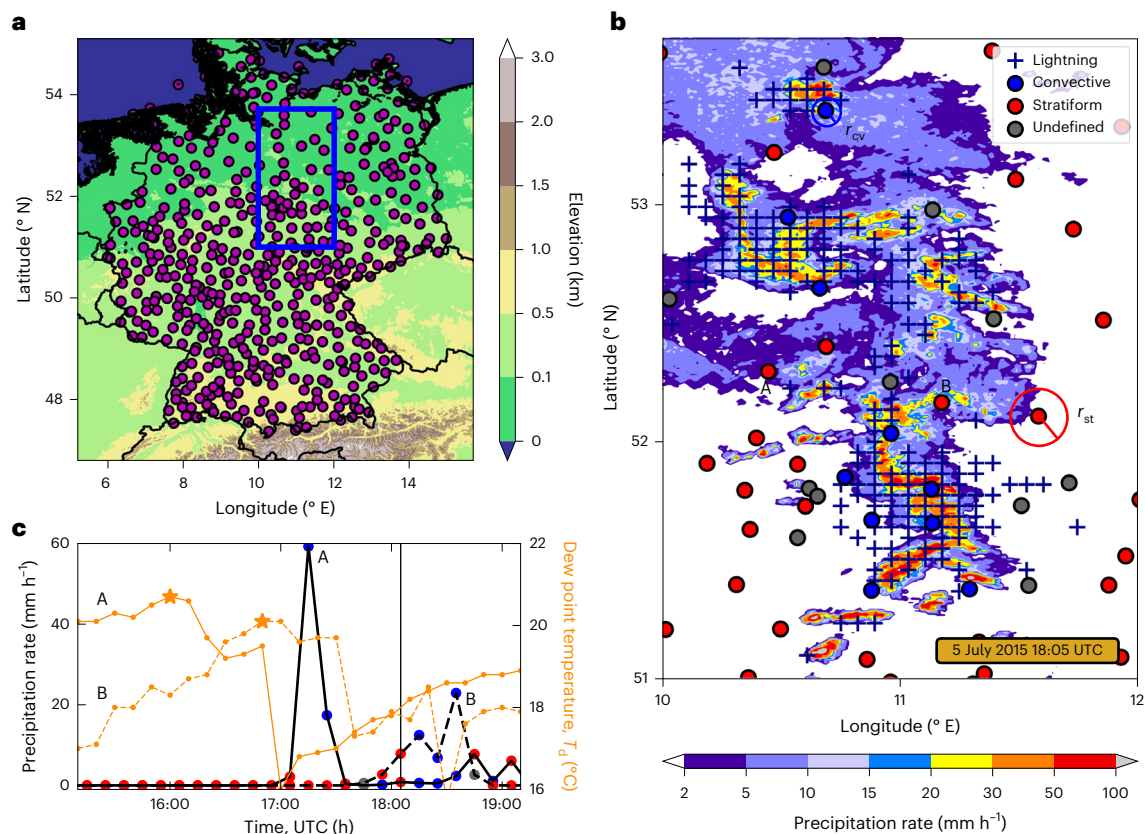


Fig. 1 | Separating convective and stratiform precipitation. **a**, In situ weather stations used in the analysis (filled magenta circles), recording 10-min precipitation and dew point temperature, super-imposed on an elevation map, which was created from the General Bathymetric Chart of the Oceans 2021 topography dataset (note the colour bar). The blue box highlights the subregion enlarged in **b**. **b**, Snapshot of radar-detected rainfall intensities (colour bar) for the subregion highlighted in **a** on 5 July 2015 at 18:05 UTC. Crosses indicate lightning occurrence between 18:00 and 18:10 UTC. Blue- and red-filled circles represent station locations with lightning occurrence within a distance r_{cv} = 5 km, classified as ‘convective’, and without lightning occurrence within a distance

r_{st} = 30 km, classified as ‘stratiform’, respectively. The data from the remaining weather stations (grey-filled circles) are not defined as belonging to either of these categories. Labels A and B refer to example time series in **c**. Example precipitation time series (black) for stations indicated in **b** by corresponding symbols (solid for A, dashed for B), with colour markers representing classifications into convective, stratiform and undefined records. Orange curves show corresponding dew point temperature time series (right vertical axis). Orange stars highlight maximum dew point temperatures relevant for the precipitation records at 18:10 UTC (grey vertical line) (Methods).

Extended Data Fig. 7), and applying our detection method to the generated statistical data, we show that the CC scaling of unclassified events (Extended Data Fig. 6a,c) is indeed possible under the underlying CC assumptions for both convective and stratiform precipitation.

Sensitivity to the definition of convective precipitation

One may ask which resolution is high enough to quantify the scaling of convective-type precipitation extremes. To explore this, we now systematically vary the resolution by adjusting the radius r_{cv} within which CG lightning is detected. Successful detection of CG lightning within an area of radius r_{cv} during a time interval τ_{cv} = 10 min qualifies this area as convective type. Allowing r_{cv} to range from 5 km to 300 km while keeping τ_{cv} = 10 min, we plot the curve $P_{99}(T_d)$ for various values of r_{cv} (Fig. 3a). Visually, the curves, displayed using a logarithmic vertical scale, show a systematic increase in slope as the radius is increased, that is, when the condition on convection is made more lenient. For the smallest available r_{cv} = 5 km, the dependence on T_d is very close to a CC increase. For larger r_{cv} , the curves become steeper, especially at the higher values of T_d , where systematic exceedence of the CC rate is visually apparent.

To summarize this systematic steepening, we derive the mean rate of increase for each of the curves. We observe a gradual increase of the mean slopes from approximately 0.9 CC for r_{cv} = 5 km to approximately

1.5 CC for r_{cv} = 300 km (Fig. 3b). The increase is such that the mean slope can no more be qualified as CC for radii exceeding 20 km (at the 95% confidence level).

To further strengthen our point, we also recomputed and plotted the scaling of extreme convective precipitation as defined by Molnar et al. (2015)¹² and Berg et al. (2013)²³ (Fig. 3c), showing that the coarse spatio-temporal definition of convective precipitation indeed results in the statistical super-CC rate found in these previous studies. We thereby mimic the scaling of Berg et al. (2013)²³ by selecting 10-min precipitation accumulations for which at least one CG lightning flash was detected within less than 50 km—representing a rough mean of the surface synoptic observation spatial resolution in Germany—over a 3-h time window centred on the respective 10-min precipitation time point. A comparison of the scaling found in Berg et al. (2013)²³ with the corresponding scaling at 10-min temporal resolution shows that coarser temporal definition of convective precipitation may further enhance the super-CC scaling.

Analogously, we also evaluate the effect of increasing the radius r_{st} used in the definition of stratiform precipitation and observe a gradual decrease of the mean slopes from approximately $1.5 \times$ CC at 5 km to approximately CC at 300 km (Fig. 2b). These findings underscore that unambiguous separation of convective-type from stratiform-type precipitation requires very strict conditioning on lightning, where lightning must occur within the immediate vicinity, that is, few km and

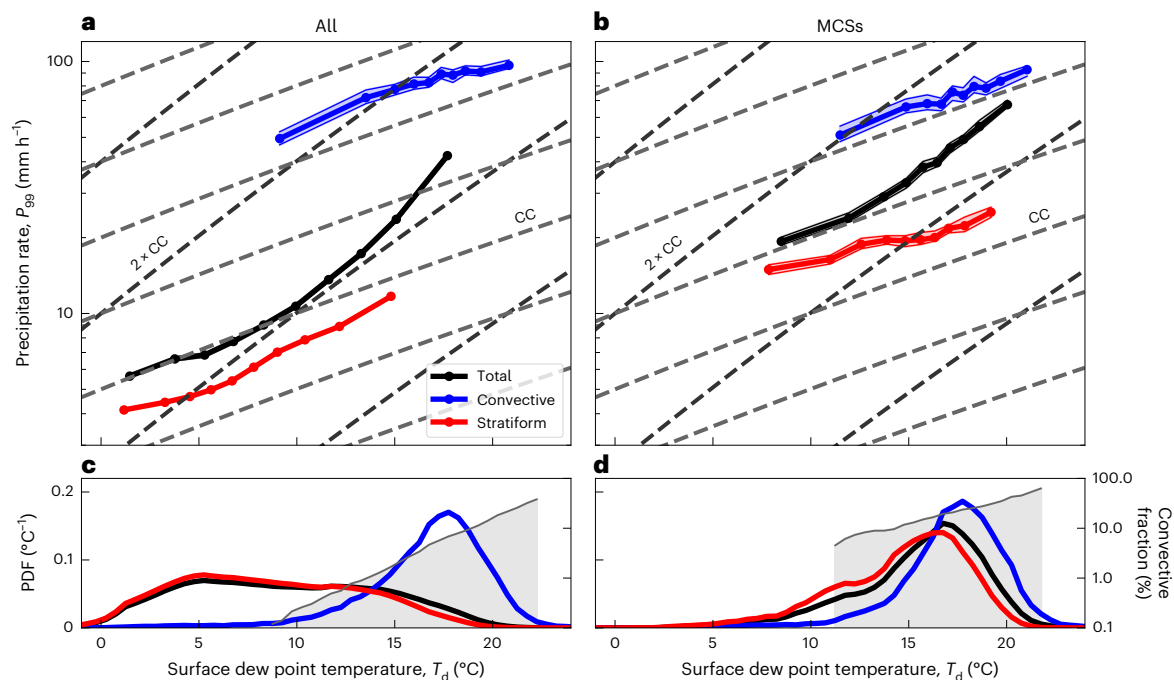


Fig. 2 | Scaling of precipitation extremes with surface dew point temperature. **a**, $P_{99}(T_d)$ for rainfall classified as convective (blue), using $r_{cv} = 5$ km, stratiform (red), $r_{st} = 300$ km and $\tau_{st} = 3$ h, and all precipitation (black). Data are presented as the 99th percentile with 95% confidence intervals (shadings) estimated using a non-parametric method based on the binomial distribution and its normal approximation for large sample sizes (Methods). Dashed light and dark grey curves indicate $1 \times CC$ and $2 \times CC$ rates (Methods). **b**, Analogous to **a** but conditional on rainfall within MCSs using $r_{cv} = 10$ km. For the stratiform type,

$r_{st} = 30$ km and $\tau_{st} = 10$ min were used. The black curve represents all precipitation within MCSs, irrespective of lightning flashes. **c**, Normalized histograms (PDF, probability density functions) for each of the three types shown in **a**. Shaded grey area indicates convective fraction (right vertical axis; note the logarithmic scale). **d**, Analogous to **c** but conditioned on precipitation within MCSs. The convective fraction curves shown in **c** and **d** increase at rate of $\approx 41\% \text{ } ^\circ\text{C}^{-1}$ and $\approx 25\% \text{ } ^\circ\text{C}^{-1}$ (respectively) with T_d . Note the logarithmic vertical axis scaling in **a** and **b** and **c** and **d**, right axis.

less than 10 min, from a precipitation measurement for the convective type. For unambiguous separation of the stratiform type, lightning must not occur in the mesoscale vicinity. Otherwise, the statistical mix of types will appear as a super-CC increase.

Repeating this analysis using hourly accumulated precipitation—a common accumulation interval in climate models—shows similar behaviour but a higher (<10 km) spatial resolution is required to properly separate convective from stratiform precipitation and obtain a CC scaling (Extended Data Fig. 8). Consistent with earlier studies^{7,12,31}, the scaling rates derived from air temperatures are significantly lower than when using dew point temperatures, although comparable resolution dependence exists (Extended Data Fig. 9).

Scaling for individual storms

The above analysis makes the point that neither convective- nor stratiform-type precipitation extremes exceed the CC rate when taken by themselves. Thus, there is no detectable mechanistic effect by which either of the two types intensifies more rapidly than expected from thermodynamics. Yet precipitation impacts society also as a statistical blend of these two precipitation types, in particular during times when MCSs pass over metropolitan areas. For MCSs, changes in the statistical contribution from convective versus stratiform sub-areas may well affect their precipitation footprint generated over human settlements—making the difference between flooding or not.

Using a recent algorithm for detecting MCSs over Europe²⁶, we therefore revisit the question of extreme rainfall scaling, now restricting to areas within MCS. The overall finding is that MCSs contain a blend of convective- and stratiform-type precipitation, but the individual CC-like scaling still holds for either of the two types alone (Fig. 2b). Taking both types together, a clear super-CC scaling is found, thus

indicating that MCSs, as a whole, deliver disproportionately more intense rainfall as T_d increases. This increase is explained by examining the proportion of convective versus stratiform-type precipitation within MCSs as T_d is varied (Fig. 2d): larger T_d makes the occurrence of convective-type precipitation more likely, even when conditioning on MCSs. Thus, a given MCS, taken as an entity, is expected to yield much more intense rainfall at higher T_d , in accordance with a super-CC increase of MCS mean intensity.

Analysing all rain events (or storms) perceived by a given fixed observer, we further describe extremes by means of rainfall IDF curves, which are widely used in hydrology to assess flood risk. The obtained IDF curves distinguish storms preceded by high T_d (15–20 °C) to those preceded by lower T_d (10–15 °C) (Methods). These curves show an increase in extreme (5-year return period) storm mean precipitation with warming (Fig. 4a). This increase is particularly pronounced and exceeds the CC rate for storm durations of 15–60 min, for which the increase in storm convective fraction (Fig. 4b) has the greatest impact on the storm mean intensity with warming. On the contrary, the storm mean intensity of long-duration (> 60 min) storms only increases at a CC or sub-CC rate. These results were found to be insensitive to the return period when varying it from 1 to 5 years and to the width of the T_d bins.

Implications for impact modelling of extreme precipitation

Global warming has been suggested to bring widespread precipitation intensification⁶, in particular regarding convective rainfall extremes⁵. Super-CC increases have served as a possible explanation for such anticipated intensification^{4,32}. The current work calls into question if the suggested super-CC increase in convective precipitation extremes actually has a mechanistic base by which thunderstorm cells come

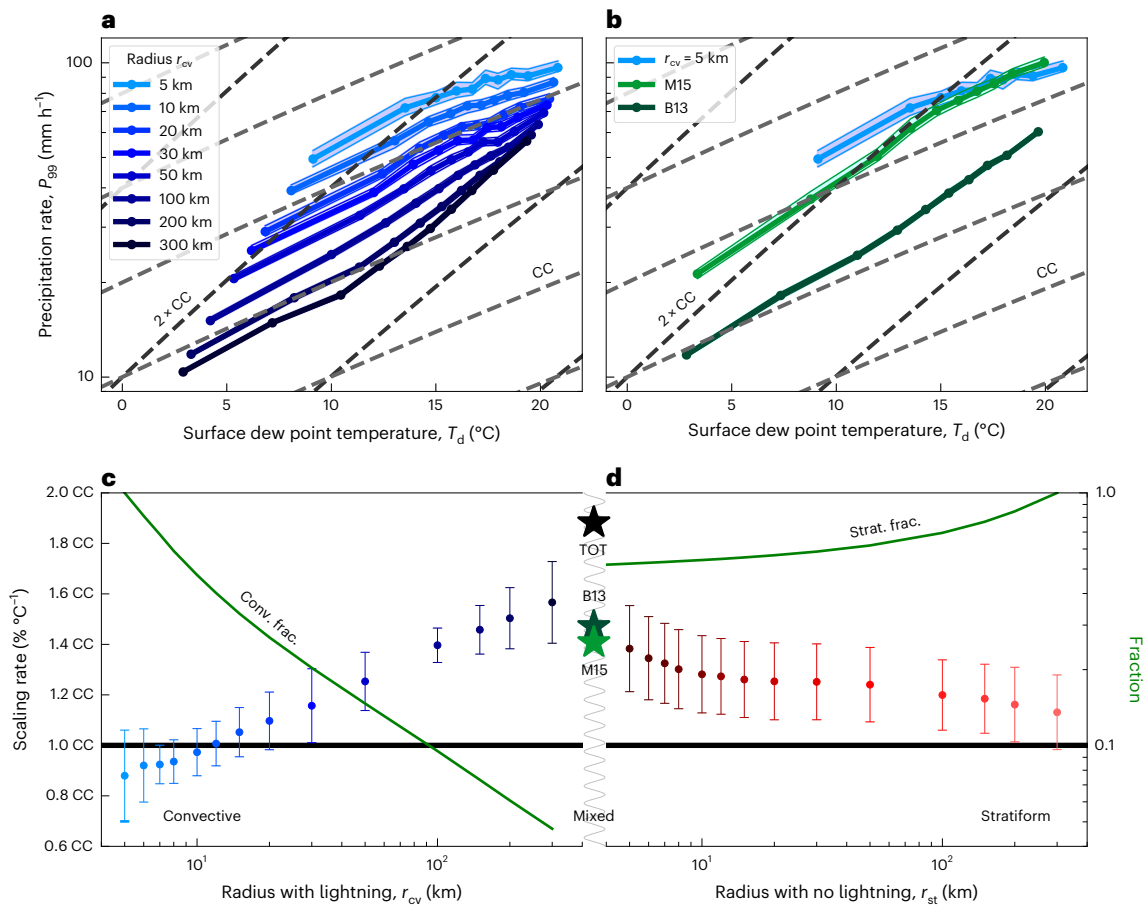


Fig. 3 | Sensitivity of extreme scaling to detection radius. **a**, Analogous to Fig. 2a but for varying detection radius r_{cv} (legend shows colour coding). **b**, Statistical consistency with previously published super-CC results: M15¹², using a maximum intensity criterion over a precipitation event; mimicking B13²³, using $r_{cv} = 50$ km and $\tau_{cv} = 3$ h; the light-blue curve is a replication of the $r_{cv} = 5$ km curve shown in **a** (Methods). **c**, Mean slopes of the curves in **a** (calculated over 10 data points), which correspond to decreasing values of r_{cv} , in shades of dark to light blue. Purely convective cases lie to the left of the plot, that is, small r_{cv} . The green curve indicates the convective fraction (Conv. frac.) corresponding to each r_{cv} .

d, Analogous to **c** but for r_{st} , that is, purely stratiform cases lie to the right of the plot. The green curve indicates the stratiform fraction (Strat. frac.) corresponding to each r_{st} . Star symbols between panels **c** and **d** indicate the mean slopes for all precipitation (TOT; Fig. 2a, black curve), and M15 and B13 (shown in **b**). Note the logarithmic vertical axis scaling in **a**, **b** and **c** (right axis) and the logarithmic horizontal axis scaling in **c** and **d**. Data in **c** and **d** are represented as mean values \pm an error estimate based on the mean of the squared residuals from a linear fit to 10 data points (Methods).

with invigorated intensities beyond the thermodynamic rate at higher temperatures^{11,22,23}. The present data unambiguously show that there is no exceedence of the CC rate at the scale of individual convective cells. To the contrary, the CC rate is a robust predictor of the change in convective precipitation intensity with temperature. Super-CC changes with temperature are found only as a statistical superposition of distinct rainfall types¹⁹.

Under such statistical superposition, precipitation clusters comprising both convective and stratiform precipitation, such as MCSs^{24,26}, could exceed CC scaling as a statistical ensemble. Societal impacts resulting from MCSs, such as flash flooding^{2,3} in increasingly urbanized watersheds¹, could be amplified under a statistical super-CC scaling. Our analysis based on IDF curves indeed suggests that it is at the flash flood scale, on the order of 15–60 minutes, where storms show strongest super-CC increases. Probing whether convective fraction increases at similar exponential rates in state-of-the-art km-scale climate change simulations would be a logical next step. Such cloud-resolving simulations are also appropriate in detecting thunderstorm events in the spatio-temporal simulation output fields and conditionally analysing the scaling of convective vs stratiform contributions. Precipitation extremes may increase at different rates at different times of the year, as the partitioning into stratiform and convective contributions differs

from season to season (Extended Data Fig. 10). Yet, current climate model projections may not accurately reproduce seasonal changes, as showcased by projections that underestimate the inland advection of wintertime maritime systems and the convective fraction of winter storms³³.

Given the current findings, refocusing the target of extreme precipitation modelling might be useful: with convective and stratiform components individually scaling along the thermodynamic CC rate, the focus could be shifted to unveiling the spatial organization of thunderstorms within mesoscale cloud fields. A strongly clustered thunderstorm population within a given MCS could locally lead to a severe flash flood whereas a scattered population would give rise to moderate, more widespread precipitation at the mesoscale. With the high-resolution simulation data now becoming available^{34,35}, detecting changes in clustering with temperature will be feasible. Prominent mechanisms for thunderstorm self-organization, such as cold pool interactions, are now heavily studied, often in idealized settings^{36–41}. Conceptual understanding, gained from such works, should find its way into realistic regional-scale studies to help inform future changes in organized convection, for example, convective processes within winter storms and large slow-moving summer systems, which may be more frequent in a warmer climate^{33,42,43}.

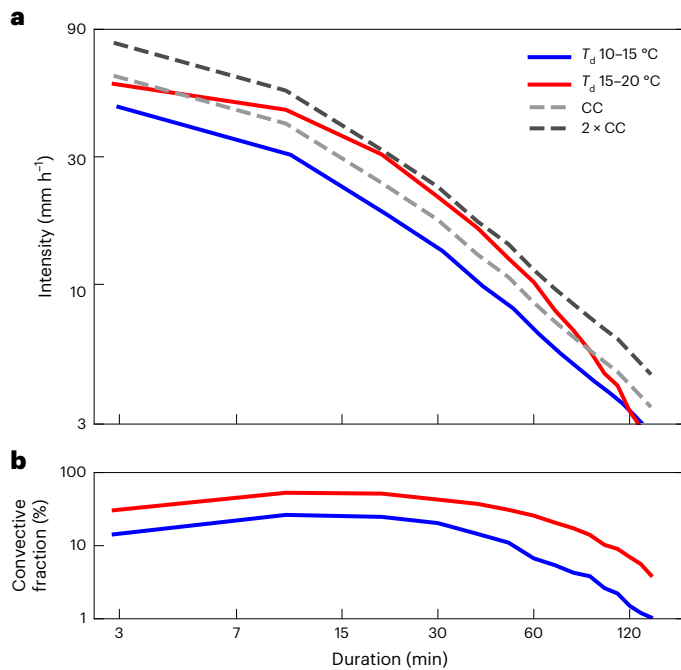


Fig. 4 | Scalings for storm mean intensities. **a**, IDF curves for the 5-year return period for storms preceded by T_d between 10 °C and 15 °C (blue) and for storms preceded by T_d between 15 °C and 20 °C (red). Dashed light and dark grey curves indicate $1 \times CC$ and $2 \times CC$ rates relative to the blue line. **b**, Averaged convective fraction as a function of storm duration for each of the two storm categories shown in **a**. Note the double-logarithmic axis scaling in both panels (Methods).

Online content

Any methods, additional references, Nature Portfolio reporting summaries, source data, extended data, supplementary information, acknowledgements, peer review information; details of author contributions and competing interests; and statements of data and code availability are available at <https://doi.org/10.1038/s41561-025-01686-4>.

References

- Hapuarachchi, H., Wang, Q. & Pagano, T. A review of advances in flash flood forecasting. *Hydrol. Process.* **25**, 2771–2784 (2011).
- Llasat, M. C. et al. Flash flood evolution in north-western Mediterranean. *Atmos. Res.* **149**, 230–243 (2014).
- Llasat, M. C., Marcos, R., Turco, M., Gilabert, J. & Llasat-Botija, M. Trends in flash flood events versus convective precipitation in the Mediterranean region: the case of Catalonia. *J. Hydrol.* **541**, 24–37 (2016).
- Kendon, E. J. et al. Heavier summer downpours with climate change revealed by weather forecast resolution model. *Nat. Clim. Change* **4**, 570–576 (2014).
- Lehmann, J., Coumou, D. & Frieler, K. Increased record-breaking precipitation events under global warming. *Clim. Change* **132**, 501–515 (2015).
- Guerreiro, S. B. et al. Detection of continental-scale intensification of hourly rainfall extremes. *Nat. Clim. Change* **8**, 803–807 (2018).
- Fowler, H. J. et al. Anthropogenic intensification of short-duration rainfall extremes. *Nat. Rev. Earth Environ.* **2**, 107–122 (2021).
- Trenberth, K. E. Conceptual framework for changes of extremes of the hydrological cycle with climate change. *Clim. Change* **42**, 327–339 (1999).
- Allen, M. R. & Ingram, W. J. Constraints on future changes in climate and the hydrologic cycle. *Nature* **419**, 224–232 (2002).
- Held, I. M. & Soden, B. J. Robust responses of the hydrological cycle to global warming. *J. Clim.* **19**, 5686–5699 (2006).
- Lenderink, G. & Van Meijgaard, E. Increase in hourly precipitation extremes beyond expectations from temperature changes. *Nat. Geosci.* **1**, 511–514 (2008).
- Molnar, P., Fatichi, S., Gaál, L., Szolgay, J. & Burlando, P. Storm type effects on super Clausius–Clapeyron scaling of intense rainstorm properties with air temperature. *Hydrol. Earth Syst. Sci.* **19**, 1753–1766 (2015).
- Ivancic, T. J. & Shaw, S. B. A U.S.-based analysis of the ability of the Clausius–Clapeyron relationship to explain changes in extreme rainfall with changing temperature. *J. Geophys. Res. Atmos.* **121**, 3066–3078 (2016).
- Park, I.-H. & Min, S.-K. Role of convective precipitation in the relationship between subdaily extreme precipitation and temperature. *J. Clim.* **30**, 9527–9537 (2017).
- Lenderink, G., Mok, H., Lee, T. & Van Oldenborgh, G. Scaling and trends of hourly precipitation extremes in two different climate zones—Hong Kong and the Netherlands. *Hydrol. Earth Syst. Sci.* **15**, 3033–3041 (2011).
- Ali, H., Peleg, N. & Fowler, H. J. Global scaling of rainfall with dewpoint temperature reveals considerable ocean-land difference. *Geophys. Res. Lett.* **48**, e2021GL093798 (2021).
- Loriaux, J. M., Lenderink, G., Roode, S. R. D. & Siebesma, A. P. Understanding convective extreme precipitation scaling using observations and an entraining plume model. *J. Atmos. Sci.* **70**, 3641–3655 (2013).
- Singleton, A. & Toumi, R. Super-Clausius-Clapeyron scaling of rainfall in a model squall line. *Q. J. R. Meteorol. Soc.* **139**, 334–339 (2013).
- Haerter, J. O. & Berg, P. Unexpected rise in extreme precipitation caused by a shift in rain type? *Nat. Geosci.* **2**, 372–373 (2009).
- Allan, R. P., Soden, B. J., John, V. O., Ingram, W. & Good, P. Current changes in tropical precipitation. *Environ. Res. Lett.* **5**, 025205 (2010).
- Berg, P. & Haerter, J. Unexpected increase in precipitation intensity with temperature—a result of mixing of precipitation types? *Atmos. Res.* **119**, 56–61 (2013).
- Lenderink, G. & Van Meijgaard, E. Unexpected rise in extreme precipitation caused by a shift in rain type? *Nat. Geosci.* **2**, 373–373 (2009).
- Berg, P., Moseley, C. & Haerter, J. O. Strong increase in convective precipitation in response to higher temperatures. *Nat. Geosci.* **6**, 181–185 (2013).
- Houze, R. A. Stratiform precipitation in regions of convection: a meteorological paradox? *Bull. Am. Meteorol. Soc.* **78**, 2179–2196 (1997).
- Houze, R. A. 100 years of research on mesoscale convective systems. *Meteorol. Monogr.* **59**, 1–17.54 (2018).
- Da Silva, N. A. & Haerter, J. O. The precipitation characteristics of mesoscale convective systems over Europe. *J. Geophys. Res. Atmos.* **128**, e2023JD039045 (2023).
- Houze Jr, R. A. Observed structure of mesoscale convective systems and implications for large-scale heating. *Q. J. R. Meteorol. Soc.* **115**, 425–461 (1989).
- Chan, S. C. et al. Large-scale dynamics moderate impact-relevant changes to organised convective storms. *Commun. Earth Environ.* **4**, 8 (2023).
- Houze Jr, R. A. Structures of atmospheric precipitation systems: a global survey. *Radio Sci.* **16**, 671–689 (1981).
- MacGorman, D. R. et al. The timing of cloud-to-ground lightning relative to total lightning activity. *Mon. Weather Rev.* **139**, 3871–3886 (2011).
- Lenderink, G., Barbero, R., Loriaux, J. M. & Fowler, H. J. Super-Clausius–Clapeyron scaling of extreme hourly convective precipitation and its relation to large-scale atmospheric conditions. *J. Clim.* **30**, 6037–6052 (2017).

32. Westra, S. et al. Future changes to the intensity and frequency of short-duration extreme rainfall. *Rev. Geophys.* **52**, 522–555 (2014).
33. Kendon, E. J. et al. Greater future U.K. winter precipitation increase in new convection-permitting scenarios. *J. Clim.* **33**, 7303–7318 (2020).
34. Schär, C. et al. Kilometer-scale climate models: prospects and challenges. *Bull. Am. Meteorolog. Soc.* **101**, E567–E587 (2020).
35. Fuhrer, O. et al. Near-global climate simulation at 1 km resolution: establishing a performance baseline on 4888 GPUS with COSMO 5.0. *Geosci. Model Dev.* **11**, 1665–1681 (2018).
36. Böing, S. An object-based model for convective cold pool dynamics. *Math. Clim. Weather Forecasting* **2**, 43–60 (2016).
37. Schlemmer, L. & Hohenegger, C. Modifications of the atmospheric moisture field as a result of cold-pool dynamics. *Q. J. R. Meteorol. Soc.* **142**, 30–42 (2016).
38. Moseley, C., Hohenegger, C., Berg, P. & Haerter, J. O. Intensification of convective extremes driven by cloud–cloud interaction. *Nat. Geosci.* **9**, 748–752 (2016).
39. Haerter, J. O. & Schlemmer, L. Intensified cold pool dynamics under stronger surface heating. *Geophys. Res. Lett.* **45**, 6299–6310 (2018).
40. Haerter, J. O., Böing, S. J., Henneberg, O. & Nissen, S. B. Circling in on convective organization. *Geophys. Res. Lett.* **46**, 7024–7034 (2019).
41. Haerter, J. O., Meyer, B. & Nissen, S. B. Diurnal self-aggregation. *npj Clim. Atmos. Sci.* **3**, 30 (2020).
42. Berthou, S. et al. Convection in future winter storms over northern Europe. *Environ. Res. Lett.* **17**, 114055 (2022).
43. Tradowsky, J. S. et al. Attribution of the heavy rainfall events leading to severe flooding in western Europe during July 2021. *Clim. Change* **176**, 90 (2023).
44. Becker, R. & Behrens, K. Quality assessment of heterogeneous surface radiation network data. *Adv. Sci. Res.* **8**, 93–97 (2012).
45. Schulz, W., Diendorfer, G., Pedeboy, S. & Poelman, D. R. The European lightning location system EUCLID – part 1: performance analysis and validation. *Nat. Hazards Earth Syst. Sci.* **16**, 595–605 (2016).
46. Poelman, D. R., Schulz, W., Diendorfer, G. & Bernardi, M. The European lightning location system EUCLID – part 2: observations. *Nat. Hazards Earth Syst. Sci.* **16**, 607–616 (2016).
47. Bartels, H. et al. *Projekt RADOLAN Routineverfahren zur Online-Aneicherung der Radarniederschlagsdaten mit Hilfe von automatischen Bodenniederschlagsstationen (Ombrometer)* (Deutscher Wetterdienst, 2004).

Publisher's note Springer Nature remains neutral with regard to jurisdictional claims in published maps and institutional affiliations.

Open Access This article is licensed under a Creative Commons Attribution 4.0 International License, which permits use, sharing, adaptation, distribution and reproduction in any medium or format, as long as you give appropriate credit to the original author(s) and the source, provide a link to the Creative Commons licence, and indicate if changes were made. The images or other third party material in this article are included in the article's Creative Commons licence, unless indicated otherwise in a credit line to the material. If material is not included in the article's Creative Commons licence and your intended use is not permitted by statutory regulation or exceeds the permitted use, you will need to obtain permission directly from the copyright holder. To view a copy of this licence, visit <http://creativecommons.org/licenses/by/4.0/>.

© The Author(s) 2025

Methods

Observational data

We use the meteorological station dataset from the German Weather Service (Deutscher Wetterdienst, DWD) observational network⁴⁴. Specifically, we extract 10-min accumulated precipitation and 2-m dew point temperature (T_d) measurements from 514 meteorological stations covering Germany (Fig. 1a) for the period between 2005 and 2020. We only retain data that have undergone routine quality control and correction^{48,49}.

The radar data are the Radar online adjustment (RADOLAN,⁴⁷) quality-controlled rainfall rate composite version RY from the DWD. This product combines 17 C-band radars covering Germany resulting in a rainfall dataset at 5-min temporal resolution with 1-km horizontal grid spacing. The rainfall rates are derived from radar reflectivity measurements following a refined radar reflectivity to rain rate relationship for liquid hydrometeors, after clutter removal and corrections accounting for topography^{47,50}.

We employ the EUCLID lightning dataset to derive convective and stratiform precipitation at high spatio-temporal resolution^{45,46}. To do so we only make use of cloud-to-ground lightning flashes (CGs), for their high (>90%) detection efficiency between 2005 and 2020⁴⁵. The number of CGs is originally provided on a $0.045^\circ \times 0.071^\circ$ (latitude–longitude) grid covering all of Germany within 10-min time windows. The location of the detected CGs is considered accurate within 500 m, which is an order of magnitude more accurate compared to the 5-km threshold used for the definition of convective precipitation. Retaining only CGs, our approach discards convective precipitation not accompanied by CG, which may somewhat affect the scaling of our defined ‘stratiform’ precipitation.

The General Bathymetric Chart of the Oceans (GEBCO) 2021 topography dataset, with a 15-arcsecond resolution, is used in Fig. 1a to assess the location of DWD weather stations relative to topography.

Extreme precipitation curves and confidence bounds

For each 10-min precipitation measurement exceeding a threshold of 0.1 mm, respectively 0.05 mm, 0.5 mm and 1 mm (Extended Data Fig. 4), we associate a corresponding dew point temperature, T_d , as the maximum T_d occurring in the three hours preceding the precipitation measurement (Figs. 2 and 3). We further condition on ‘dry’ T_d records, that is, those without measurable non-zero precipitation records, to retain the T_d corresponding to the inflow of a given precipitation system rather than its outflow which can be strongly influenced by precipitation evaporation. The pronounced diurnal cycle of the occurrence of 10-min extreme convective precipitation (Extended Data Fig. 2d) could indicate that most of this extreme convective precipitation may be driven by diurnal processes, such as those in the boundary layer and lower free troposphere. If no such dry T_d can be found in the 3 h preceding a precipitation measurement, the 10-min precipitation record is discarded from the analysis. This method successfully retains T_d records in the warm sector of extreme convective systems (Extended Data Fig. 2a,b), where the temporal variations of T_d remain of modest amplitude (<2 °C; Extended Data Fig. 2c), which reduces potential attribution errors. We also discard all 10-min precipitation records that are preceded by temperatures not exceeding 5 °C in the 3 h preceding the precipitation measurement, to exclude potential inconsistencies in the derived $P_{90}(T_d)$ related to snowfall occurrence. The selected values of T_d are then corrected to account for the different altitudes of the weather stations, assuming a dry adiabatic lapse rate, to the sea level and a constant specific humidity. After this selection, a total of nearly 137 years of precipitation and T_d pairs are formed. At this step, further conditioning is made to retain convective, stratiform or MCS precipitation (below).

Once the final selection is made, we distribute the resulting pairs into ten bins sorted by T_d , where each bin contains the same number of samples and where we additionally ensure a minimum of 500 samples

per bin. For each bin, we then compute the mean T_d and associate it with the 99th percentile, respectively, the 90th, 95th and 99.5th percentiles in Extended Data Fig. 3, of 10-min precipitation intensities exceeding the chosen threshold. The ten resulting pairs describe the T_d –precipitation extreme relationship used in this study. We explore the effect of defining fixed T_d bin widths of 2 °C each on the obtained scaling rates in Extended Data Fig. 5.

Following the non-parametric confidence intervals described in the literature⁵¹ (equations (13) and (14)), we estimate a confidence interval—at the 95% confidence level—on these precipitation percentiles as follows: extracting a number of samples, N , from the true distribution of precipitation, the number of elements that exceed the true q th precipitation percentile follows a binomial distribution $\mathcal{B}_{N,1-q}$. If one assumes that the binomial distribution can be approximated by a normal distribution (because N is large), a confidence interval on the q th percentile can be derived as:

$$\Pr\{q - \alpha\} < \Pr\{q\} < \Pr\{q + \alpha\} \quad (1)$$

$$\alpha = 1.96 \times \sqrt{q(1-q)/N}. \quad (2)$$

Here \Pr denotes the distribution of the N precipitation samples, and the numbers enclosed in curly parentheses represent the percentiles of evaluation. For the case of fixed T_d bin widths (Extended Data Fig. 5), we further calculate an effective number of samples for deriving the confidence intervals. Indeed, the correlation of the 10-min precipitation records within bins having a low number of samples leads to an important underestimation of the confidence intervals when the total number of samples is used to derive confidence intervals. The effective number of samples is calculated assuming that the correlation coefficient between two 10-min precipitation measurements recorded by two different stations at two different time steps is a linear function of the distance separating these stations and of the time interval between these two measurements. Two precipitation measurements are set as uncorrelated if the time interval or the distance between these two measurements exceeds an hour or 50 km, respectively.

The August–Roche–Magnus approximation for saturated vapour pressure ($e_{\text{sat}}(T_d)$) is used to derive the Clausius–Clapeyron scaling rates as a function of T_d (in degrees Celsius):

$$e_{\text{sat}}(T_d) = 610.94 \exp\left(\frac{17.625T_d}{243.04 + T_d}\right). \quad (3)$$

The sensitivity to the precipitation percentile and threshold is explored in Extended Data Figs. 3 and 4.

To derive the mean slopes of the precipitation-extremes–dew-point-temperature relationships in Fig. 3 and Extended Data Figs. 8 and 9, we fit a straight line to the ten data points using a weighted least squares regression. The weights account for the range of temperature values each point represents, with each point weighted by half the distance between its neighbouring temperature points (with edge points adjusted accordingly). The linear fit is performed on the logarithm of the precipitation values. To account for uncertainty, we calculate error bars from the residuals of the fit. Specifically, we estimate the variance by averaging the squared residuals and use its square root to adjust the slope at both ends of the fitted line, providing upper and lower bounds of the scaling rate.

IDF curves

The IDF curves were computed by defining storms as a time series of 10-min precipitation measurements that each exceed a threshold of 0.1 mm, allowing for gaps with a maximum duration of 10 min. For each storm, the storm mean precipitation intensity is calculated by dividing the total storm precipitation accumulation by its duration. In this, we assumed that the maximum likelihood that a storm spans n time steps

of $dt = 10$ min each is reached for storm durations $d = n \times dt - 10$ min. We therefore defined storm durations as $d = n \times dt - 10$ min for storms spanning n time steps. As an exception, storms spanning only one time step were given a duration $d = 2.88$ min, which corresponds to the best match between the extrapolated IDF curves towards the lowest storm durations and the storm mean intensity values retrieved using this duration. Storms were divided into two categories ($10^\circ\text{C} \leq T_d \leq 15^\circ\text{C}$ and $15^\circ\text{C} \leq T_d \leq 20^\circ\text{C}$) according to the maximal T_d values reached within the three hours preceding their onset and conditioned on 'dry' (as defined previously) T_d records. The dashed light and dark grey lines in Fig. 4 were obtained by multiplying the 5-year return intensity in the lower dew point temperature category by a CC or $2 \times$ CC scaling accounting for the mean dew point temperature differences between the upper and lower dew point temperature category in each duration bin and according to equation (3).

Classification scheme

We define convective, respectively stratiform, 10-min precipitation using the distances r_{cv} , respectively r_{st} , from the nearest EUCLID CG detected within a centred time window τ_{cv} , respectively τ_{st} . If a CG is detected within less than $r_{cv} = 5$ km from a station within a centred time window $\tau_{cv} = 10$ min, the station precipitation is considered as convective (Extended Data Fig. 1), irrespective of whether lightning occurs outside this radius r_{cv} . If no CG is detected within less than $r_{st} = 300$ km from a station within a centred time window $\tau_{st} = 180$ min, the station precipitation is considered as stratiform. The remainder of the precipitation, which consists of non-CG precipitation events evolving in a convective environment, is flagged as 'undefined.' In the main text, convective fraction is defined as the ratio between the number of 10-min precipitation measurements flagged as convective and the total number of 10-min precipitation measurements.

MCS detection

To define MCS precipitation, we first identify and track RADOLAN precipitation features (defined as contiguous areas of non-zero precipitation in a four-pixel neighbourhood; PFs) using the algorithm presented in Da Silva and Haerter (2023)²⁶ with minor modifications accounting for changes in spatio-temporal resolution as described in the following. Whereas we retained the temporal 5-min RADOLAN outputs, we regridded the RADOLAN spatial precipitation field to a 0.1° grid, which improves the likelihood of spatial overlap and thus the tracking of fast moving precipitation systems. The definition of MCS is similar to that in Da Silva and Haerter (2023), substituting the 30-min with the 10-min CG lightning dataset, which improves the detection accuracy. We also increased the PF detection threshold from 2 mm h^{-1} to 4 mm h^{-1} to account for the change from the spatio-temporally smoothed Integrated Multi-satellitE Retrievals for GPM (IMERG) precipitation field to the instantaneous and local measure of precipitation from RADOLAN. For the same reasons, and to ensure sufficient precipitation and T_d pair records, the condition on the minimum duration for which an MCS has a diameter that exceeds 100 km was reduced from four to one hour. MCS pixels are thus defined at a 5-min interval on a 0.1° grid. We then consider the station location and the 10-min temporal window of measurement. A station 10-min accumulated precipitation measurement is considered as emerging from an MCS when the regridded 0.1° RADOLAN gridbox containing the station, or any of the four nearest neighbours of this RADOLAN gridbox, is part of an identified MCS PF at any time point within the corresponding 10-min time window, that is, either at $t = 0$, $t = 5$ or $t = 10$ min from the beginning of the 10-min window. As selecting MCS precipitation considerably reduces the precipitation and T_d pair records, we loosen the criteria for defining convective and stratiform precipitation within MCSs to ensure statistical significance of the scaling derived. Indeed, for the MCS convective and stratiform classification, we use $r_{cv} = r_{st} = 20$ km and $\tau_{cv} = 10$ min and $\tau_{st} = 10$ min, respectively.

Statistical model

We employ a simple statistical model to discuss the realism and potential implications of our results. The underlying main assumptions of this model are that both convective and stratiform precipitation scale at CC and that the convective fraction increases exponentially at a rate of $41\% \text{ }^\circ\text{C}^{-1}$. We then generate synthetic precipitation data for different dew point temperatures as follows: first, we consider a fixed number of lightning strikes and place them in a square area in the middle of a two-dimensional square domain (Extended Data Fig. 7a). Consistent with the EUCLID dataset, the lightning strikes are separated by a distance of 4 km to one another. Second, we vary the domain size to achieve a targeted lightning density that increases exponentially at a rate of $41\% \text{ }^\circ\text{C}^{-1}$, as found in the observations (Fig. 2a,c). This procedure is numerically equivalent to increasing the number of lightning clusters at a fixed domain size. We use our method based on the distance to the closest lightning strike (Extended Data Fig. 1) to classify all grid points into the convective, unclassified and stratiform categories. Each of the defined convective, stratiform and unclassified categories may contain a mix of convective-type and stratiform-type precipitation. We assume that the probability of finding convective-type precipitation around each lightning strike decreases with the distance from this lightning strike (Extended Data Fig. 7b). Specifically, in our model, the probability that rainfall occurring at a given position is of convective type, given that the nearest lightning strike occurs a distance r from it, $P_{\text{conv}}(r)$, is given by the Gaussian probability distribution

$$P_{\text{conv}}(r) = \exp\left(-\frac{r^2}{2\sigma^2}\right) \quad (4)$$

where we used $\sigma = 15$ km to achieve consistency with the observed precipitation intensities of the unclassified data points. Using this spatial probability distribution, we are able to calculate the expected number of grid points with convective precipitation for each category. Dividing by the total number of grid points of each category, we obtain an expected convective fraction for each category. We then generate convective and stratiform precipitation data, assuming that they follow an exponentially decaying distribution with a scale parameter that increases according to the CC relationship. This ensures that the 99th percentile, and, more generally, all percentiles, of the generated convective and stratiform precipitation, follows the CC relationship. To reproduce the observed precipitation intensity differences between convective and stratiform precipitation, we assume a ratio of eight between the scale parameter of convective precipitation and that of stratiform precipitation. We distribute the generated convective and stratiform precipitation in the three categories in accordance with the convective fractions derived from the spatial probability distribution (equation (4)). For each temperature bin (here increasing by steps of 1°C), we constrain the total number of precipitation data so that the final dew point temperature normalized histogram (black curve in Extended Data Fig. 6c) approaches the one of the observations (black curve in Extended Data Fig. 6d). The resulting extreme precipitation curves show great consistency with those of the observations (Extended Data Fig. 6a vs Extended Data Fig. 6b). This simple model could also be used at the scale of MCSs, by scaling down both the central lightning cluster size and the radius R_{st} , which would yield similar results.

Data availability

The meteorological station dataset is available online at https://open-data.dwd.de/climate_environment/CDC/observations_germany/climate/10_minutes/ (DWD)⁴⁴. The RADOLAN precipitation dataset is available at <https://www.cen.uni-hamburg.de/icdc/data/atmosphere/samd-ltfd-datasets/hdfd-miub-drnet00-l3-rr.html>. The BLIDS/EUCLID lightning data are not publicly available due to privacy restrictions but may be provided upon request. Requests should be sent to BLIDS/

EUCLID (contact: w.schulz@ove.at), specifying the intended use and complying with a data-use agreement. Response times typically range up to 2 weeks. The GEBCO 2021 topography dataset can be downloaded at https://www.gebco.net/data_and_products/historical_data_sets/. Source data are provided with this paper.

Code availability

The code used to prepare data, derive statistics and plot figures is available via GitHub at <https://github.com/Nicolas-A-Da-Silva/SuperClausiusShiftRainType/> under the Apache 2.0 license.

References

48. Kaspar, F. et al. Monitoring of climate change in Germany - data, products and services of Germany's National Climate Data Centre. *Adv. Sci. Res.* **10**, 99–106 (2013).
49. Spengler, R. *The new quality control and monitoring system of the Deutscher Wetterdienst*. Instruments and Observing Methods Report No. 75, 245–248 (World Meteorological Organization, 2002).
50. Weigl, E. *Hoch aufgelöste Niederschlagsanalyse und -vorhersage auf der Basis quantitativer Radar- und Ombrometerdaten für grenzüberschreitende Flusseinzugsgebiete von Deutschland im Echtzeitbetrieb* Technical Report Version 2.5.7 (Deutscher Wetterdienst, 2023).
51. Ialongo, C. Confidence interval for quantiles and percentiles. *Biochem. Med.* **29**, 5–17 (2019).

Acknowledgements

We gratefully acknowledge a grant from the European Research Council (ERC) under the European Union's Horizon 2020 research and innovation programme (grant number 771859, J.O.H.) and the Novo Nordisk Foundation Interdisciplinary Synergy Program (grant number NNF19OC0057374, J.O.H.). We acknowledge resources of the Deutsches Klimarechenzentrum (DKRZ), granted by its Scientific Steering Committee (WLA) under project ID bb1166. We thank H. Pichler and W. Schulz for kindly preparing and providing the EUCLID data set. We also thank the Integrated Climate Data Center (ICDC), Centrum für Erdsystemforschung und Nachhaltigkeit (CEN),

University of Hamburg for the support and Institute of Geosciences of the University of Bonn, Germany, for the provision of the RADOLAN dataset (<https://www.cen.uni-hamburg.de/icdc/data/atmosphere/samd-ltfd-datasets/hdfd-miub-drnet00-l3-rr.html>). We thank H. Fowler for valuable reviewer comments to our paper and are especially grateful for her suggestion to explore how the IDF curves are influenced by super-CC scaling. The topography data were supplied by the General Bathymetric Chart of the Oceans: GEBCO Compilation Group (2021): GEBCO 2021 Grid (<https://doi.org/10.5285/c6612cbe-50b3-0cff-e053-6c86abc09f8f>).

Author contributions

J.O.H. and N.A.D.S. conceived and designed the study. N.A.D.S. collected the datasets and performed the computations. J.O.H. and N.A.D.S. contributed to the interpretation of the results. J.O.H. and N.A.D.S. wrote the manuscript.

Funding

Open access funding provided by Leibniz-Zentrum für Marine Tropenforschung (ZMT) GmbH.

Competing interests

The authors declare no competing interests.

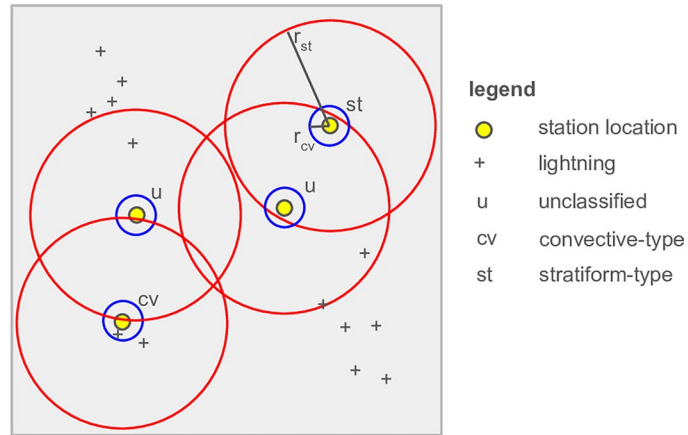
Additional information

Extended data is available for this paper at <https://doi.org/10.1038/s41561-025-01686-4>.

Correspondence and requests for materials should be addressed to Nicolas A. Da Silva.

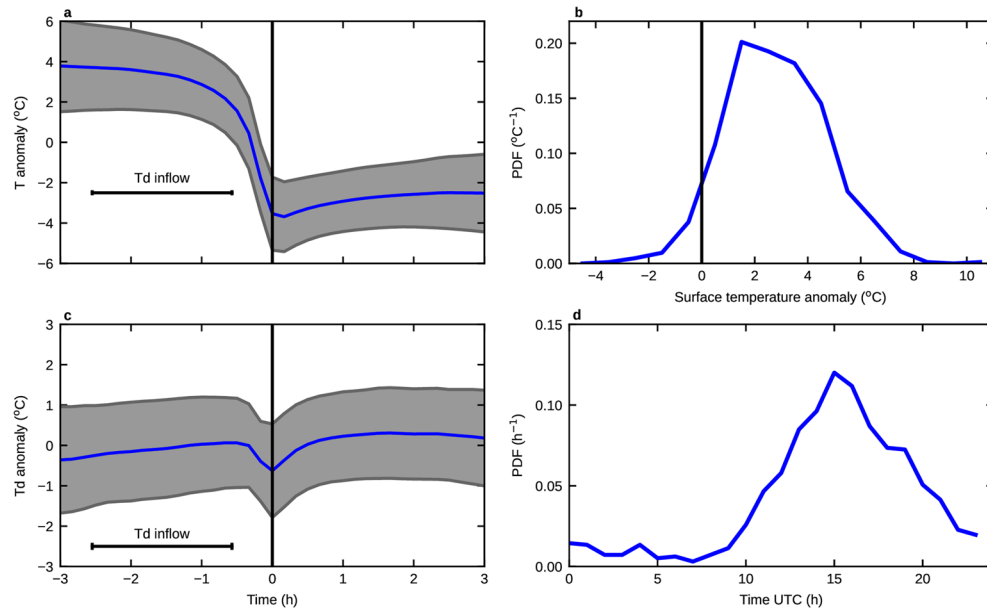
Peer review information *Nature Geoscience* thanks Hayley Fowler and the other, anonymous, reviewer(s) for their contribution to the peer review of this work. Primary Handling Editor: Tom Richardson, in collaboration with the *Nature Geoscience* team.

Reprints and permissions information is available at www.nature.com/reprints.



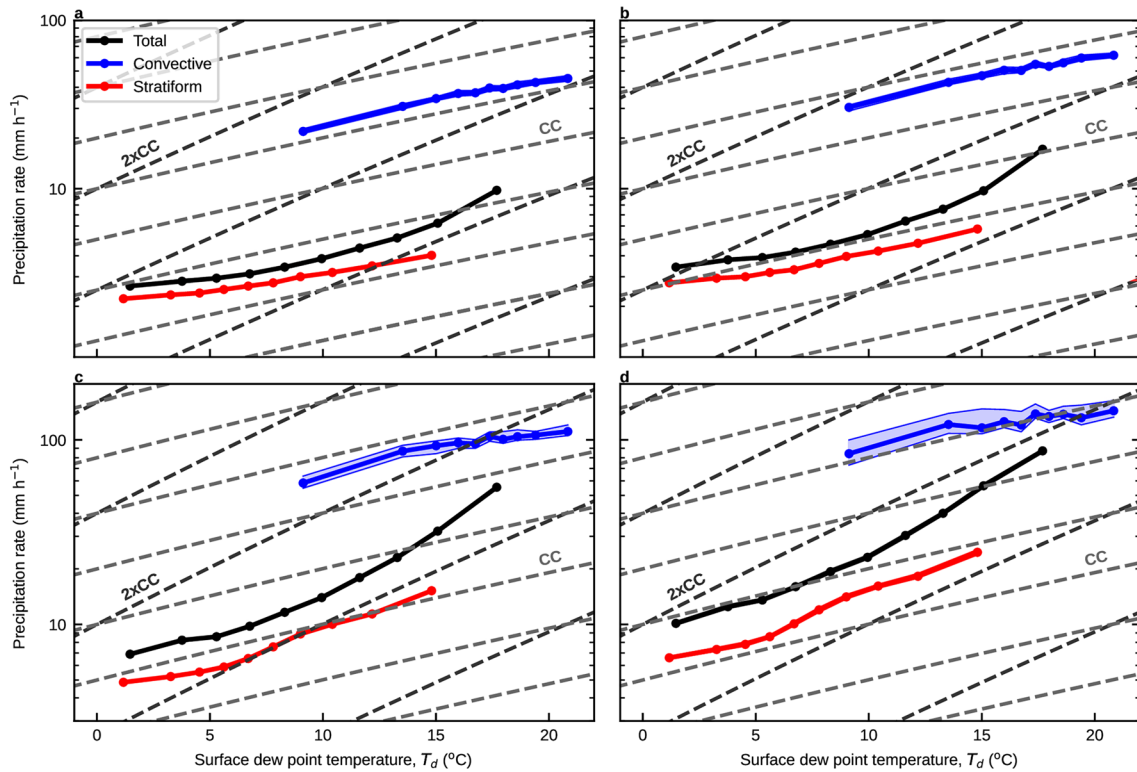
Extended Data Fig. 1 | Schematic describing the classification procedure. Station locations (yellow), lightning occurrences (plus-symbols) and rainfall types, as described in legend. The radii of r_{st} (large red circles) and r_{cv} (small blue circles) are indicated in the schematic for one case. Note that one st-type station

exists, where no lightning was detected within a circle of radius r_{st} , one cv-type station exists, where lightning occurred within a circle of radius r_{cv} , and two u-type stations exist, where lightning existed within r_{st} but not within r_{cv} from the stations (*Details: Methods*).



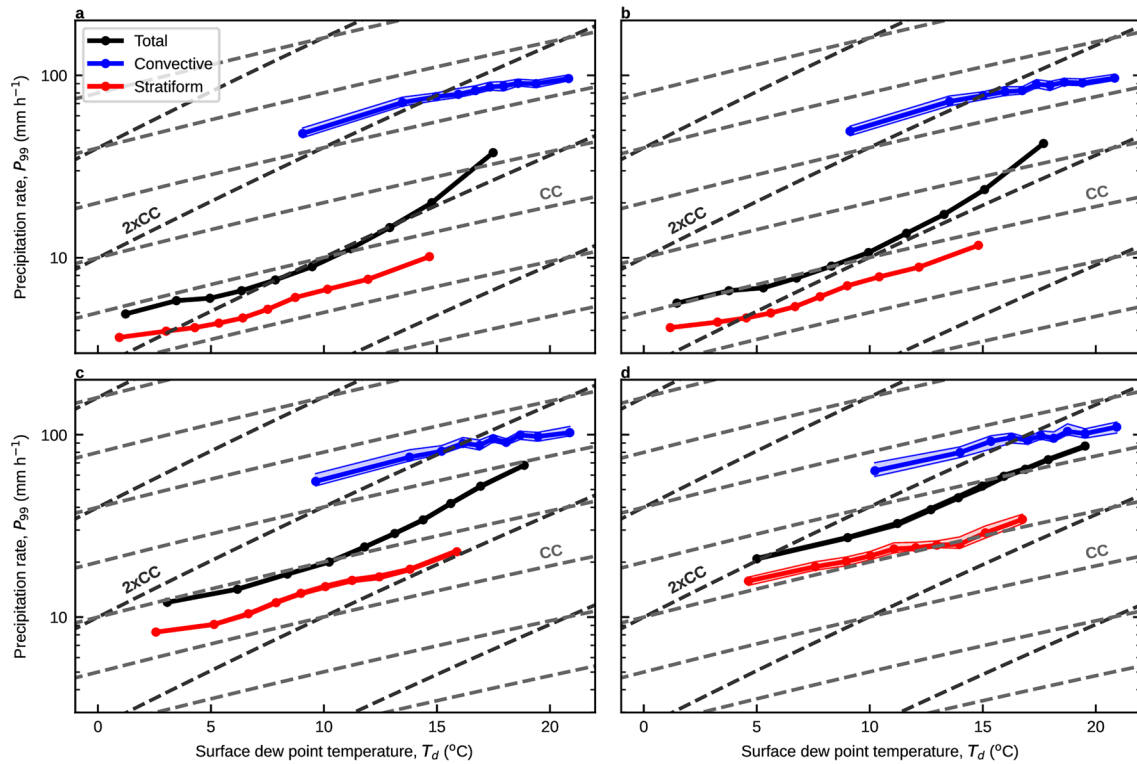
Extended Data Fig. 2 | Statistics for 10-minute extreme convective precipitation events. Averaged time series of (a), surface temperature (T) anomaly, and (c), surface dew point temperature (T_d) anomaly around 10-minute extreme convective precipitation periods (black vertical line, at $t=0$). The anomalies were computed from a 6-hour mean centred on the 10-minute extreme precipitation time. The grey shading areas indicate the spread of the

anomalies (plus and minus one standard deviation). The horizontal segment is centred on the mean T_d retained for the analysis and has a width of two standard deviations. Normalised histograms (PDF) of, (b), T anomalies at the point in time of the retained T_d , and (d), of the hour (UTC) when the 10-minute extreme convective precipitation occurs. The black vertical line in (b) indicates the 0°C anomaly.



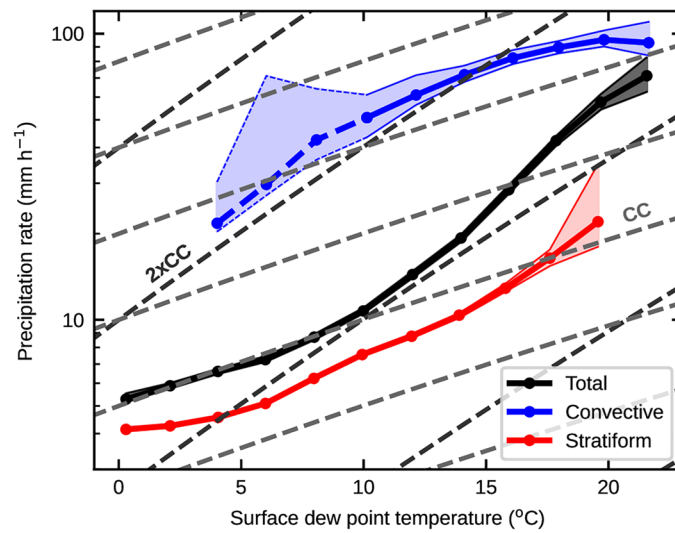
Extended Data Fig. 3 | Sensitivity to percentile in the definition of extremes. Analogous to Fig. 2a but using the 90th (a), 95th (b), 99.5th (c), and 99.9th percentiles (d), thus modifying the percentile used to define extreme precipitation. **Data are presented as the 90th (respectively 95th, 99.5th,**

99.9th) percentile with 95% confidence intervals (shadings) estimated using a non-parametric method based on the binomial distribution and its normal approximation for large sample sizes (Details: Methods). Note the change in y-axis range between panels a, b and panels c, d.



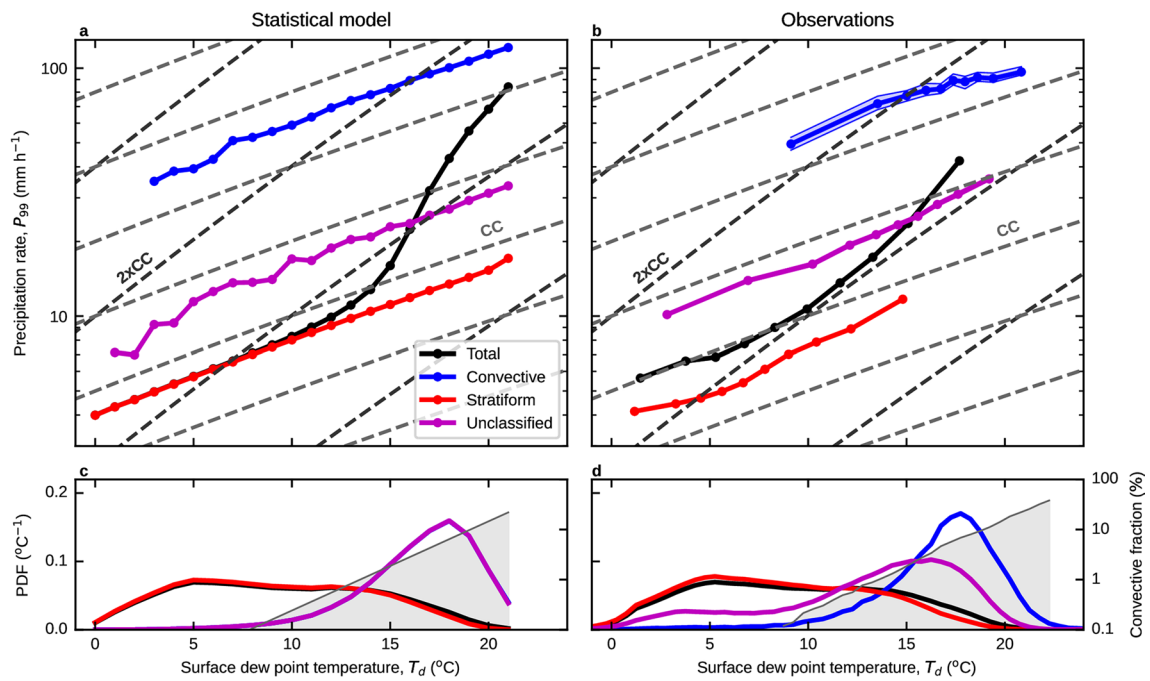
Extended Data Fig. 4 | Sensitivity to the precipitation threshold. Analogous to Fig. 2a but selecting 10-minute precipitation records exceeding 0.05 mm (a), 0.1 mm (b), 0.5 mm (c), and 1 mm (d), thus modifying the precipitation threshold. Data are presented as the 99th percentile with 95% confidence intervals

(shadings) estimated using a non-parametric method based on the binomial distribution and its normal approximation for large sample sizes (*Details: Methods*).



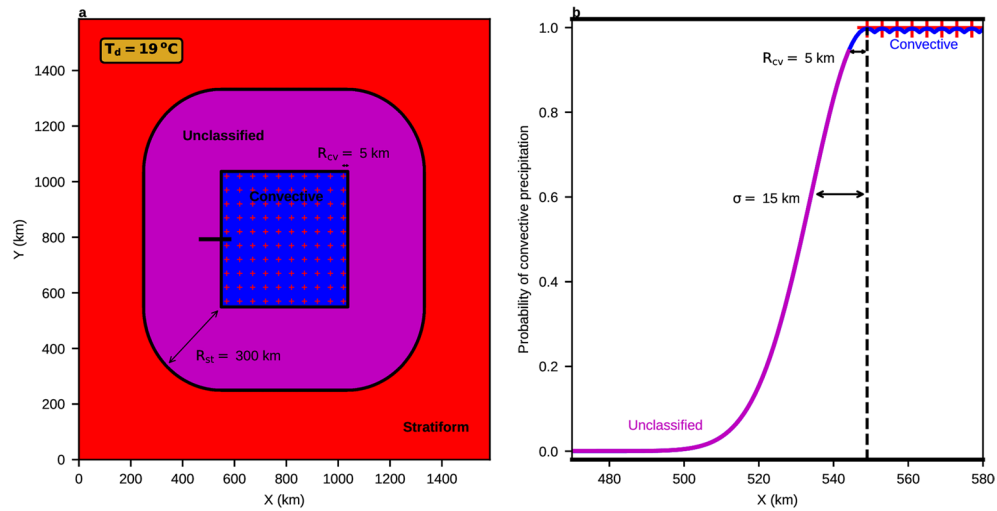
Extended Data Fig. 5 | Scaling for fixed bin widths. Analogous to Fig. 2a but using fixed T_d bin widths. The curve for convective precipitation extremes below $T_d < 10^\circ\text{C}$ is unreliable (see the error bars) and is therefore represented in a dashed blue line on an indicative basis. **Data are presented as the 99th percentile**

with 95% confidence intervals (shadings) estimated using a non-parametric method based on the binomial distribution and its normal approximation for large sample sizes (Details: Methods).



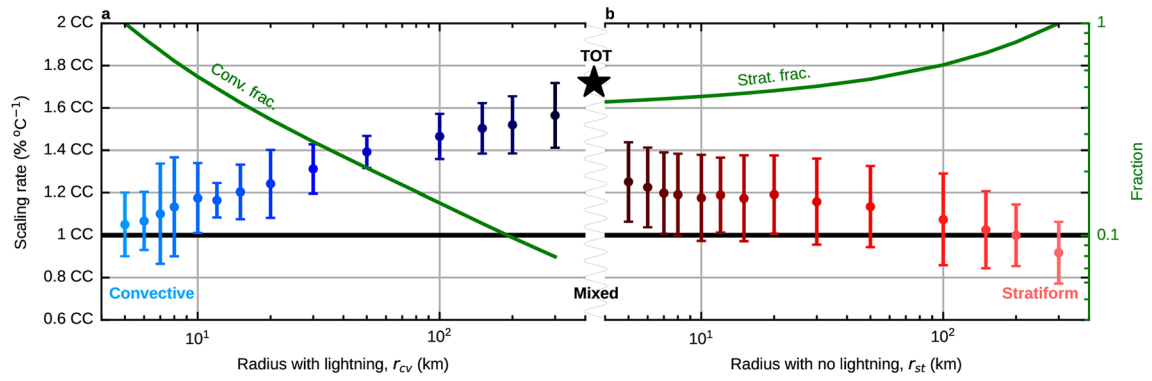
Extended Data Fig. 6 | Scaling for the statistical model. Analogous to Fig. 2 but for the statistical model (a, c) and observations (b, d; corresponding to Fig. 2a, c). We additionally show the scalings and normalised histograms of the unclassified events (magenta). The magenta and blue curves coincide in panel c. Allowing for stronger clustering at high dew point temperatures in our simple model would separate the magenta and blue curves in panel c, but would only produce little

changes for the slope of the unclassified precipitation intensity with dew point temperature (magenta curve in a). **Data are presented as the 99th percentile with 95% confidence intervals (shadings) estimated using a non-parametric method based on the binomial distribution and its normal approximation for large sample sizes (Details: Methods).**

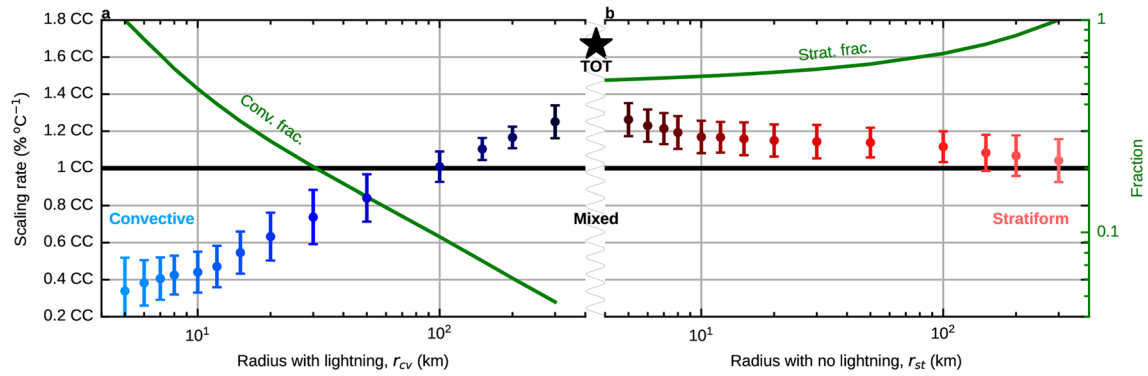


Extended Data Fig. 7 | Spatial distributions in the statistical model. Stratiform (red), unclassified (magenta), and convective (blue) areas as defined from a densely filled spatial pattern (here chosen square for simplicity) of lightning strikes (symbolically represented by red crosses) defined in the statistical model, here for the case of $T_a = 19^\circ\text{C}$ (a). Slice, corresponding to the thick black segment at $Y = 800$ km in a, of the spatial probability distribution of convective

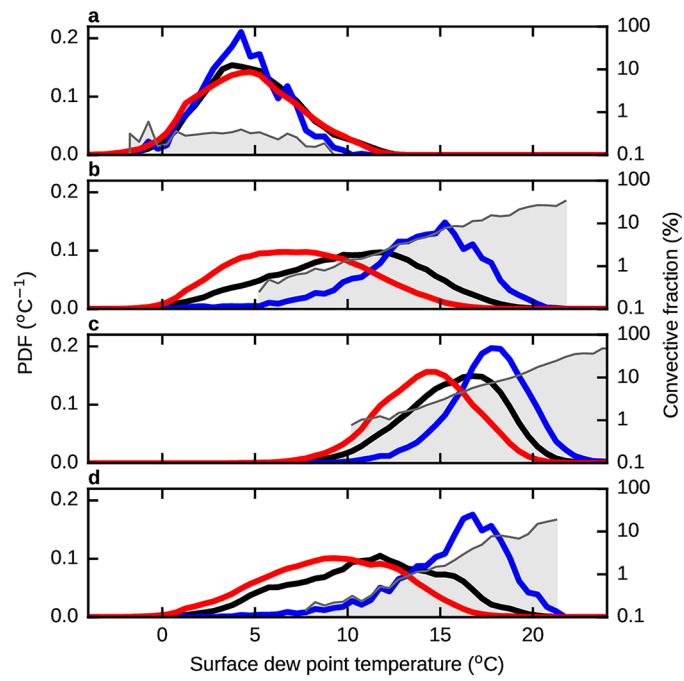
precipitation assumed in the statistical model (b). The probability decreases with the distance from the closest lightning strike (red crosses) as a Gaussian with a standard deviation set as $\sigma = 15$ km. The blue and magenta segments of this probability distribution are consistent with the location of the convective and unclassified categories (respectively). The dashed black vertical line is indicative of the location of the closest lightning strike for all $X < 549$ km (Details: Methods).



Extended Data Fig. 8 | Sensitivity of extreme scaling to the detection radius for hourly accumulations. Analogous to Fig. 3c,d but for hourly precipitation. Data in a and b are represented as mean values \pm an error estimate based on the mean of the squared residuals from a linear fit to 10 data points (*Details: Methods*).



Extended Data Fig. 9 | Sensitivity of extreme scaling with temperature to detection radius. Analogous to Fig. 3c,d but replacing dew point temperatures by temperatures. Data in a and b are represented as mean values \pm an error estimate based on the mean of the squared residuals from a linear fit to 10 data points (*Details: Methods*).



Extended Data Fig. 10 | Seasonal dependence of convective fraction. Analogous to Fig. 2c, but for (a), winter (DJF), (b) spring (MAM), (c) summer (JJA), and (d) autumn (SON).